

CM²



MAGAZINE

第 19 期



南方科技大学海洋磁学中心主编

创刊词

海洋是生命的摇篮，是文明的纽带。地球上最早的生命诞生于海洋，海洋里的生命最终进化成了人类，人类的文化融合又通过海洋得以实现。人因海而兴。

人类对海洋的探索从未停止。从远古时代美丽的神话传说，到麦哲伦的全球航行，再到现代对大洋的科学钻探计划，海洋逐渐从人类敬畏崇拜幻想的精神寄托演变成可以开发利用与科学研究的客观存在。其中，上个世纪与太空探索同步发展的大洋科学钻探计划将人类对海洋的认知推向了崭新的纬度：深海（deep sea）与深时（deep time）。大洋钻探计划让人类知道，奔流不息的大海之下，埋藏的却是亿万年的地球历史。它们记录了地球板块的运动，从而使板块构造学说得到证实；它们记录了地球环境的演变，从而让古海洋学方兴未艾。

在探索海洋的悠久历史中，从大航海时代的导航，到大洋钻探计划中不可或缺的磁性地层学，磁学发挥了不可替代的作用。这不是偶然，因为从微观到宏观，磁性是最基本的物理属性之一，可以说，万物皆有磁性。基于课题组的学科背景和对海洋的理解，我们对海洋的探索以磁学为主要手段，海洋磁学中心因此而生。

海洋磁学中心，简称 CM^2 ，一为其全名“Centre for Marine Magnetism”的缩写，另者恰与爱因斯坦著名的质能方程 $E = MC^2$ 对称，借以表达我们对科学巨匠的敬仰和对科学的不懈追求。

然而科学从来不是单打独斗的产物。我们以磁学为研究海洋的主攻利器，但绝不仅限于磁学。凡与磁学相关的领域均是我们关注的重点。为了跟踪反映国内外地球科学特别是与磁学有关的地球科学领域的最新研究进展，海洋磁学中心特地主办 CM^2 Magazine，以期与各位地球科学工作者相互交流学习、合作共进！

“海洋孕育了生命，联通了世界，促进了发展”。21世纪是海洋科学的时代，由陆向海，让我们携手迈进中国海洋科学的黄金时代

目 录

海磁文苑.....	1
关于科研的一些想法	1
岩石磁学演绎.....	3
第 9 章 磁化率概念进五阶-磁化率张量.....	3
文献导读.....	6
1. 末次间冰期全球海洋温度变化.....	6
2. 楣石和磷灰石中的氧同位素及其在地壳演化研究中的潜力	9
3. 晚第三纪末北美黄土高原突现.....	11
4. 皮托深渊 (Pito Deep) 辉长岩的结构特征揭示出快速扩张洋 中脊上深成地壳的岩浆过程和起源.....	15
5. 四国盆地半远洋沉积物的 Sr-Nd-Pb 同位素组成——对新生代 晚期黑潮搬运沉积物和菲律宾海板块运动的影响	19
6. 南半球在过去 1Ma 对南亚季风降水的驱动	23
7. 基于多旋翼无人机的低空地球物理磁勘探有望取代传统的地 面勘测.....	25
8. 利用石笋中细菌 3-羟基脂肪酸对中国中部全新世古温度和古 水文变化的重建.....	27
9. 西班牙 Busturia 的 Goikoetxe 洞穴沉积物红色着色： 对古气 候变化的指示.....	29

关于科研的一些想法

曹伟

上一次这么长的假期应该还是高考完的那个暑假。八年后的这个假期同样丰富充实。网络课程的学习在有条不紊的进行，“宅在家”也让我有时间完善自己的知识框架，同时也对科研经历有所思考和沉淀。对于“科研”，我有一些简单的认识和想法。

科研的基础是积累的过程。从本科地信专业，硕士地球物理，到博士的磁学研究，很庆幸这是一个连贯和积累的过程，地质、海洋、物探、软件以及数学物理等基础学科形成的知识体系帮助我在“这一行”不断向前。以前学习的积累就是现在研究的基础，当然这也是一个不断学习的过程。上个学期的课程中，古地磁学习使我对磁学研究有了翻天覆地的认识，空间统计学使用的Arcgis软件在测绘方面也有很好的应用，加波师兄的“python大讲堂”不断提高科研的自动化水平，这些都是在为科研积累知识和技能。

科研的价值在于创新和应用。科研要能够发现并解决问题，这就是做别人没做过的事，有所创新和突破。“无人机航母计划”试飞成功令我激动不已，数据精度数量级式提升，航测突破航程限制能够实现全球海洋覆盖，这种创新的磁测方式为海洋磁学研究提供了无限可能。

我对自己的研究方向很有信心，这主要得益于刘老师根据我的知识背景为我量身打造的研究计划，岩石磁学和海洋磁测两个方向同时进行，“两条腿走路”相辅相成。对于“阿尔金红黏土”的研究方向，我认为这是我需要练就的“基本功”，通过磁学课程、研究背景和磁学实验，掌握磁学知识和实验操作，为后续磁学研究打下良好基础；对于“海洋航测”的研究方向，能够用好已经掌握的知识 and 手段，结合“无人机航母”这一创新平台，进一步学习先进软件方法，解决新的海洋科学问题，实现突破和创新。

对于下一步工作我也有清醒的认识，目前岩石磁学实验还需要更多实验参数的支持，更重要的是对数据的处理和解释，能够解决青藏高原哪些古环境问题。

磁测方面需要掌握航测平台的基本操作和新数据的分析处理,更重要的是新数据的解释以及应用,高精度的测异常数据对于磁条带研究已经表现出突出优势,同时我会经常看着磁异常图思考,例如新的数据对于识别矿产,沉船,以及移动舰艇等方面会不会有更加丰富的应用。敢想敢干,突破创新,力争在科研道路上迈出更大一步。

第 9 章 磁化率概念进阶-磁化率张量

之前我们对磁化率的定义都是在一维上，也就是沿着外场方向 M 的变化。现在我们要把磁化率的概念进一步进阶。

对磁化率更为精确的解释需要引入张量的概念。对于一块样品，在不同方向上测量的磁化率值不一样，这叫做磁化率各向异性（Anisotropy of magnetic susceptibility, AMS）。而且，在一个方向上加场，会引起其他方向上 M 的变化，这就较为复杂了。

磁化强度和外加场这两个矢量之间的线性关系可以用二阶张量来表示。

$$M_i = \chi_{ij}H_j,$$

其中磁化率矩阵为 $\chi = \begin{pmatrix} \chi_{11} & \chi_{12} & \chi_{13} \\ \chi_{21} & \chi_{22} & \chi_{23} \\ \chi_{31} & \chi_{32} & \chi_{33} \end{pmatrix}$,

其中 j 代表外场方向， i 代表三个正交矢量方向（ X_1 、 X_2 、 X_3 ）， χ_{11} 、 χ_{22} 、和 χ_{33} 是外场在（ X_1 、 X_2 、 X_3 ）方向上沿着这三个方向的磁化率。而 χ_{ij} 则表示在一个方向加场，可以在三个正交方向产生磁化率。

该矩阵中含有 6 个独立矩阵元素。因此，只要有 6 个独立方向的磁化率测量就可以得到这 6 个矩阵元素。为了提高测量精度以及得到误差分析，通常要测量 15 个方向的磁化率。

我们用右手螺旋法则来定义三个正交方向。

在早期没有自动化旋转的磁力仪时，上述 15 步设置是最为标准的 AMS 测量方式，我们需要用手自己调节样品的位置，较为费时耗力。现在的磁化率仪器

都有了自动旋转设置，测量 AMS 就方便了很多。

通过磁化率矩阵，可以求相应的磁化率特征向量和特征值 (K_{max} , K_{int} 和 K_{min})。从而磁化率的二阶张量（磁化率各向异性）可以用磁化率椭球来表示。为了描述磁化率椭球的空间形态，前人研究定义了诸多的参数（表 1）：

表 1 磁化率椭球主要参数总结表*

参数（参考文献）	公式
特征值对数（Jelinek, 1981）	$\eta_1 = \ln \tau_1; \eta_2 = \ln \tau_2; \eta_3 = \ln \tau_3$
平均磁化率对数（Jelinek, 1981）	$\bar{\eta} = (\eta_1 + \eta_2 + \eta_3) / 3$
各向异性度（Nagata, 1961）	$P = \tau_1 / \tau_3$
校正后的各向异性（Jelinek, 1981）	$P' = \exp \sqrt{2 [(\eta_1 - \bar{\eta})^2 + (\eta_2 - \bar{\eta})^2 + (\eta_3 - \bar{\eta})^2]}$
形状因子（Jelinek, 1981）	$T = (2\eta_2 - \eta_1 - \eta_3) / (\eta_1 - \eta_3)$
磁线理（Balsley & Buddington, 1960）	$L = \tau_1 / \tau_2$
磁面理（Stacey et al., 1960）	$F = \tau_2 / \tau_3$
磁线理对数（Woodcock, 1977）	$L' = \ln(L)$
磁面理对数（Woodcock, 1977）	$F' = \ln(F)$

*其中 τ 代表磁化率特征值

这里我们需要特别澄清磁线理和磁面理只是一个比值，没有方向的概念。如果想表达磁化率长轴和短轴的方位信息，我们要用磁化率长轴（或者短轴）的倾角和偏角来表示。这个错误初学者经常会犯，要引起注意。

磁化率椭球的形状可以分为三种：三轴(Triaxial)、针状(Prolate)和饼状

(Oblate)。如果磁化率的椭球可以清晰地定义三个特征方向，我们称这种椭球为三轴椭球 ($T=0$)。如果其长轴无法定义，而短轴有明确的方向，这种椭球为饼状 ($1>T>0$)。如果长轴方向可以定义，短轴不定向，这种椭球为针状 ($0>T>-1$) (图 3)。

因为 SD 和 MD 颗粒具有完全不同的磁化率各向异性。相同的排列方式可以造成完全相反的结果。如图 4 所示，SD 颗粒的长轴（磁化率短轴）沿着 Z 轴定向排列，此时，磁化率椭球的短轴方向就沿着垂直方向，而长轴方向则无法定义，因此，对于这种分布的 SD 颗粒，会产生一个饼状磁化率椭球。如果把 SD 颗粒换成 MD，其磁化率长轴（颗粒的长轴）沿着垂向分布，而短轴无法定向，此时的磁化率椭球为针状。

如果 SD 颗粒的长轴沿着水平面均匀分布，此时其短轴，也就是磁化率的长轴统一沿着垂向分布，而短轴无定向，对应的磁化率椭球为针状。如果是 MD 颗粒，则对应着饼状。

通过以上分析可知，磁化率椭球的长短轴与磁性颗粒的长短轴分布密切相关，而后者与造成磁性颗粒定向排列的各种地质过程相关。因此，磁化率各向异性可以被用来研究相关的地质过程，比如水流方向、熔岩流流动方向、压力方向等。

正是因此磁化率各向异性的存在，在研究古地磁数据时，比如对于瓦片等考古材料（具有非常强的磁化率各向异性），需要考虑进行磁化率各向异性的校正。

文献导读

1. 末次间冰期全球海洋温度变化

翻译人：仲义 zhongy@sustech.edu.cn



S. Shackleton, D. Baggenstos, J.A. Menking, et al., *Global ocean heat content in the last interglacial* [J]. *Nature Geoscience*, 2020, 13(1), 77-81.

摘要：末次间冰期（129-116 ka）是过去 800ka 以来气候最暖阶段之一，其中海平面高度比现今高出几米。然而，在重建过程中温度的峰值和幅度各不相同，导致相对海平面的个别因素（质量增加和海水膨胀）相对重要性仍不确定。我们首次利用冰芯中惰性气泡之间的海洋温度来记录相对海平面的热膨胀公式。在倒数第二个冰消期（129 ka）平均大洋温度达到比现今高出 $1.1 \pm 0.3^\circ\text{C}$ ，导致比现今海平面高出 0.7 ± 0.3 m。然而，海洋热含量的最大值是一个瞬时特征；在末次间冰期的前几年，平均海洋温度在约 127 ka 时达到了一个稳定与现代相当的值。海洋平均温度峰值与海洋和大气环流突变的替代性指标的同步表明，海洋平均温度极大值与前一段时期大洋环流作用减弱导致海洋内部的热量堆积量有关。

ABSTRACT: The Last Interglacial (129-116 thousand years ago (ka)) represents one of the warmest climate intervals of the past 800,000 years and the most recent time when sea level was metres higher than today. However, the timing and magnitude of the peak warmth varies between reconstructions, and the relative importance of individual sources that contribute to the elevated sea level (mass gain versus seawater expansion) during the Last Interglacial remains uncertain. Here we present the first mean ocean temperature record for this interval from noble gas measurements in ice cores and constrain the thermal expansion contribution to sea level. Mean ocean temperature reached its maximum value of $1.1 \pm 0.3^\circ\text{C}$ warmer-than-modern values at the end of the penultimate deglaciation at 129 ka, which resulted in 0.7 ± 0.3 m of thermosteric sea-level rise relative to present level. However, this maximum in ocean heat content was a transient feature; mean ocean temperature decreased in the first several thousand years of the interglacial and achieved a stable, comparable-to-modern value by ~ 127 ka. The synchronicity of the peak in mean ocean temperature with proxy records of abrupt transitions in the oceanic and atmospheric circulation suggests that the

mean ocean temperature maximum is related to the accumulation of heat in the ocean interior during the preceding period of reduced overturning circulation.

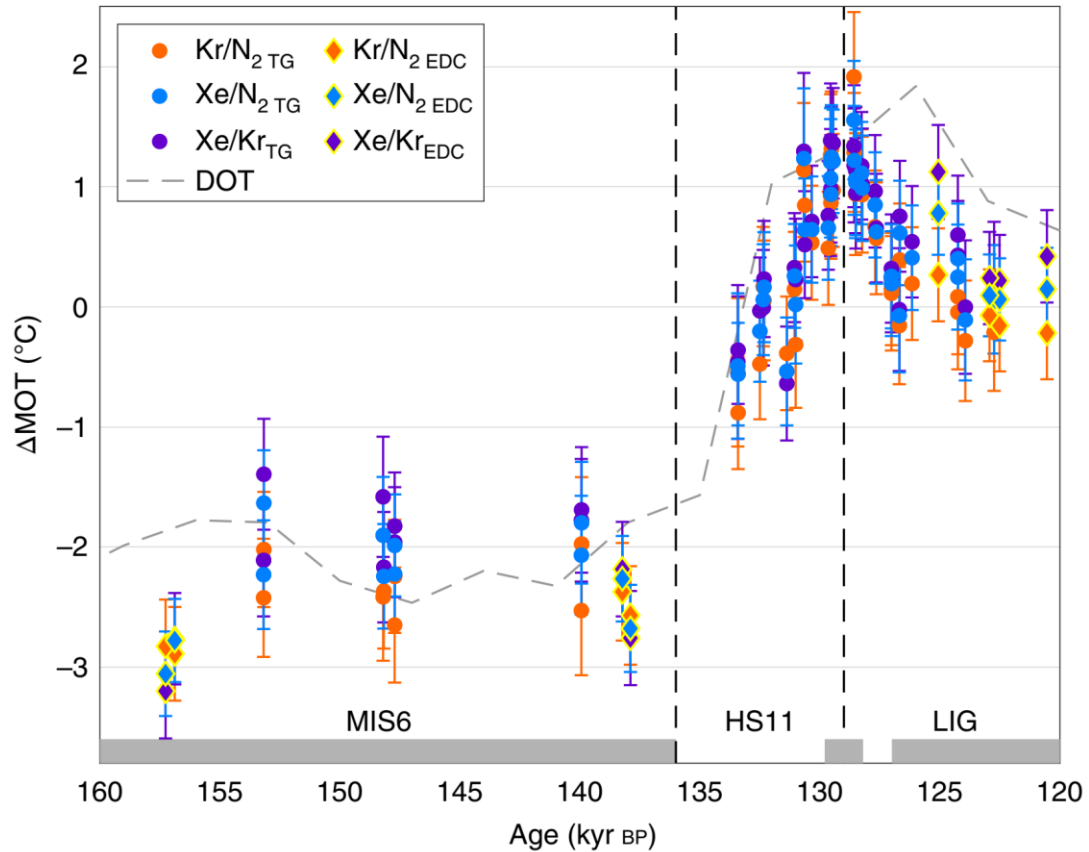


Figure 1. MoT anomaly from Kr/N₂, Xe/N₂ and Xe/Kr. MOT data are shown with 1 σ error (Methods). The grey bars indicate the time intervals for which MIS6 MOT (>136 ka), peak MOT (129.0 \pm 0.8 ka) and stable LIG MOT (<127 ka) are calculated. MOT is reported on the AICC2012 chronology. Global average deep ocean temperature (DOT) from stacked marine sediment records¹¹ on LR04 is shown for reference. kyr, thousand years.

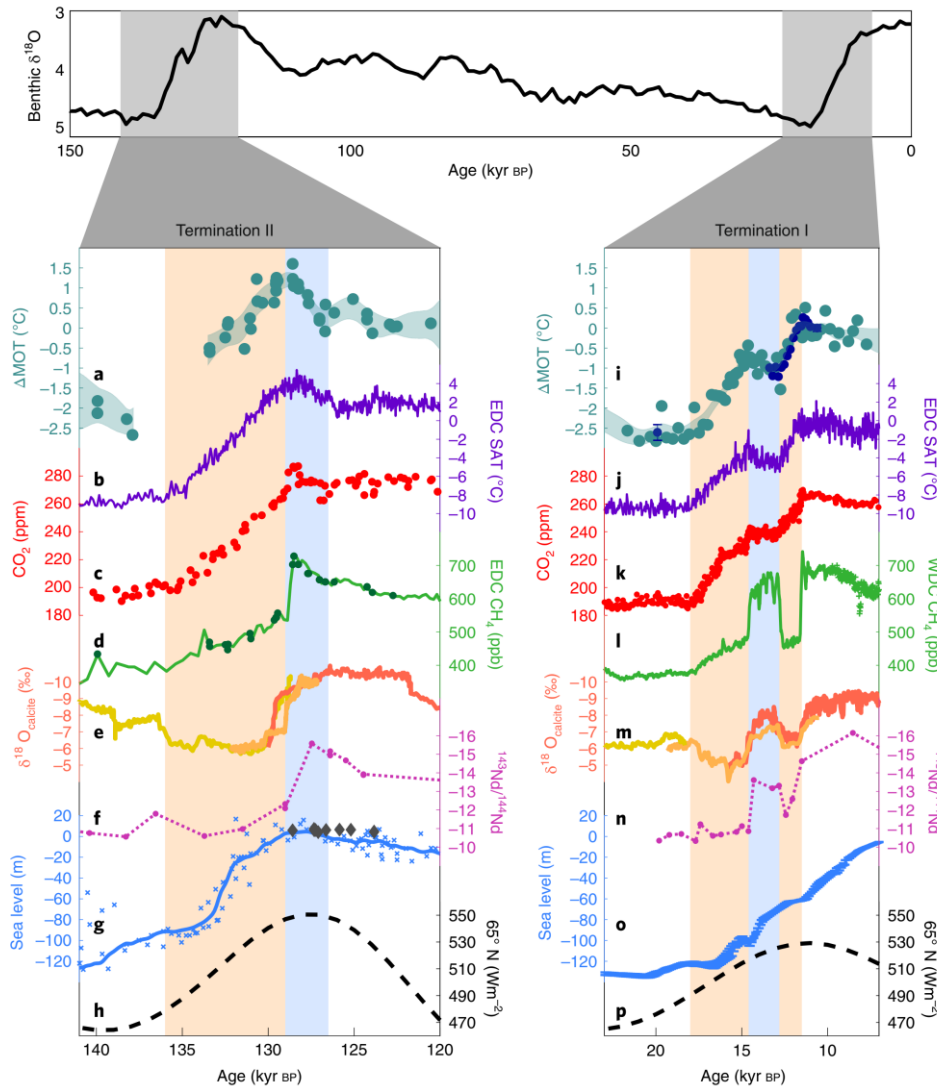


Figure 2. Climate records of Terminations II and I. a–h, Climate records of Termination II. a, MOT anomaly relative to modern from this study with 1σ error (shading). b, Antarctic temperature21 anomaly relative to the average over the past 1,000 yr. c, CO_2 . d, CH_4 . The green circles show TG CH_4 measurements. a–d are presented on AICC2012. e, Sanbao Cave ^{230}Th -dated $\delta^{18}\text{O}$ calcite records. Colours distinguish the individual speleothems. f, North Atlantic $^{143}\text{Nd}/^{144}\text{Nd}$ on a core-specific age scale. g, Red sea level corrected for isostatic effects on a core-specific age scale (light blue). The grey diamonds show coral reef sea-level records. h, Summer solstice insolation at 65°N . i–p, Climate records of Termination I. i, MOT anomaly relative to modern from the WAIS Divide (WDC) (turquoise) and TG (dark blue). Error bars show the spread (1σ) of TG replicate samples measured at Scripps Institution of Oceanography (SIO) for this study (Supplementary Information). j, As in b but for Termination I. k, CO_2 . l, CH_4 . i, k and l are presented on WD2014. m, Dongge Cave (red) and Hulu (orange and yellow) $\delta^{18}\text{O}$ calcite records. n, North Atlantic $^{143}\text{Nd}/^{144}\text{Nd}$ on core-specific age scale. o, Eustatic sea level with 1σ error from radiocarbon/uranium series-dated coral and sediment records. p, As for h. The orange bars indicate the times when the AMOC was in a weakened mode and the blue bars show periods of strong AMOC and mean ocean/Antarctic cooling. Top panel: benthic $\delta^{18}\text{O}$ on LR04. The grey bars highlight the intervals shown in a–p

2. 榍石和磷灰石中的氧同位素及其在地壳演化研究中的潜力



翻译人：冯婉仪 fengwy@sustech.edu.cn

Bruand E, Storey C, Fowler M, Heilimo E, EIMF. Oxygen isotopes in titanite and apatite, and their potential for crustal evolution research[J]. Geochimica et Cosmochimica Acta, 2019, 255: 144-162.

摘要： 锆石的氧同位素分析往往与地质年代学和 Hf 同位素分析相结合，这是了解大陆地壳演化的关键。在本文，我们通过证明副矿物（榍石和磷灰石）的氧同位素系统是可靠的，并通过建立与 O 同位素和微量元素浓度相关的地球化学指标来更好地限定岩浆的成因，从而扩大了这些副矿物的利用价值。与锆石相比，榍石和磷灰石在演化程度较低的岩浆中更常见，而且对岩浆作用和地壳变质作用的响应更强烈。我们展示来自不同地质时期花岗质岩石中的榍石、磷灰石和锆石的新数据，这些花岗质岩石包括：显生宙高 Ba-Sr 花岗岩（喀里多尼亚省，苏格兰）、太古代赞岐岩（卡累利阿省，芬兰）和新元古代玄武岩-安山岩-英安岩-流纹岩系列（BADR；Guernsey, Channel Island）。我们证明了：(i) 本文研究的副矿物的 $\delta^{18}\text{O}$ 值不受结晶分异作用的影响；(ii) $\delta^{18}\text{O}$ 在所有三个副矿物之间具有显著的相关性，这表明磷灰石和榍石可以有效地记录岩浆的 $\delta^{18}\text{O}$ ；(iii) 这些副矿物还能记录花岗质岩石在同岩浆期-岩浆期后的变质和/或流体循环事件。

ABSTRACT: Oxygen isotope analysis of zircon, often combined with geochronology and Hf isotope analysis, has been pivotal in understanding the evolution of continental crust. In this contribution, we expand the use of underexplored accessory phases (titanite and apatite) by demonstrating that their oxygen isotope systems can be robust, and by developing geochemical indicators involving O isotopes and trace element concentrations to better constrain magma petrogenesis. These minerals have the advantage over zircon of being present in less evolved magmas and being more responsive to igneous processes and crustal metamorphism. We present new data on titanite, apatite and zircon from carefully-selected granitoids through geological time: the Phanerozoic high Ba-Sr granites (Caledonian province, Scotland), Archean sanukitoids (Karelia province, Finland) and a Neoproterozoic basalt-andesite-dacite-rhyolite suite (BADR; Guernsey, Channel Island). We demonstrate: (i) that $\delta^{18}\text{O}$ values of the studied accessory minerals are not

affected by crystal fractionation, (ii) a strong correlation between $\delta^{18}\text{O}$ in all three accessory minerals, showing that apatite and titanite can faithfully record the magmatic $\delta^{18}\text{O}$; (iii) that these accessory minerals can also record metamorphic and/or fluid circulation events during the syn- to post-magmatic history of granitoids.

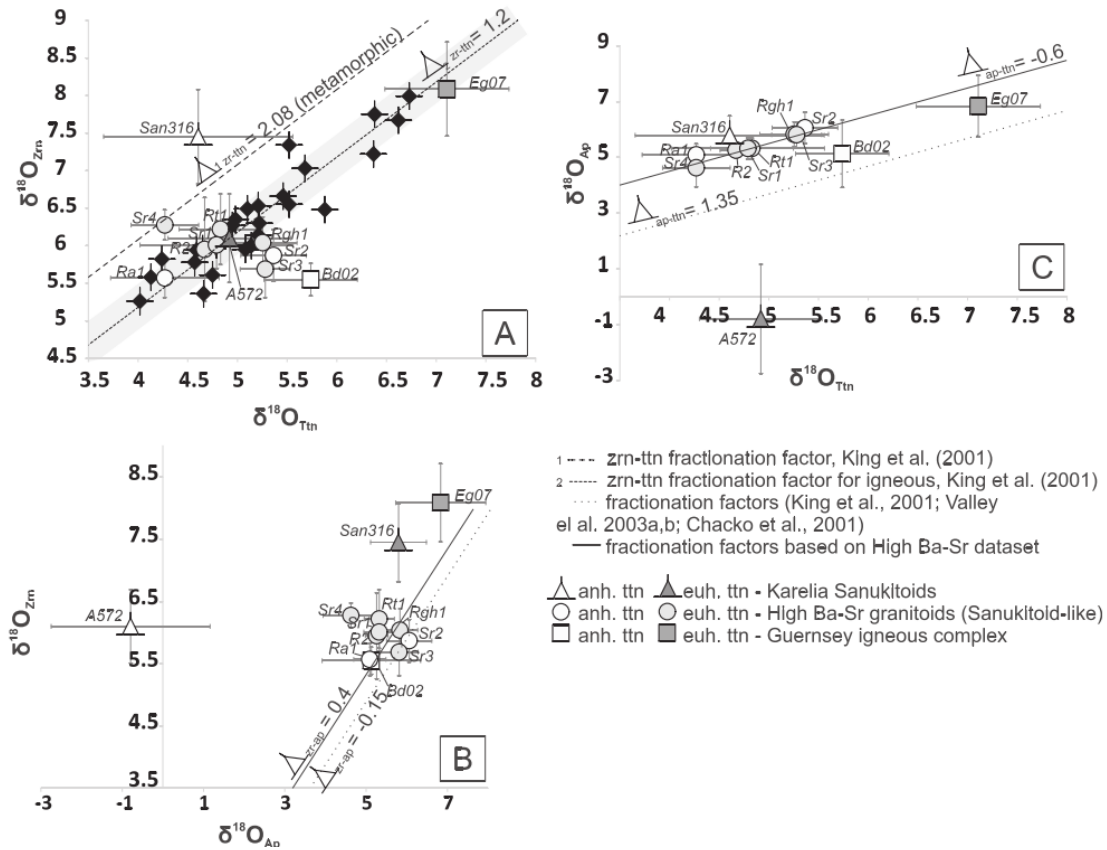


Figure 1. Compilation of apatite, titanite and zircon. $\delta^{18}\text{O}$ for the different samples studied in this contribution (Table 2). A – $\delta^{18}\text{O}_{\text{zrn}}$ vs $\delta^{18}\text{O}_{\text{ttn}}$, factor fractionation for igneous (1.2 ± 0.3 , grey field) and metamorphic rocks from the literature have been reported (King et al., 2001), B – $\delta^{18}\text{O}_{\text{zrn}}$ vs $\delta^{18}\text{O}_{\text{ap}}$, C – $\delta^{18}\text{O}_{\text{ap}}$ vs $\delta^{18}\text{O}_{\text{ttn}}$. Fractionation factors for the High Ba-Sr dataset are calculated based on the average of all High Ba-Sr samples.

3. 晚第三纪末北美黄土高原突现



翻译人: 蒋晓东 jiangxd@sustech.edu.cn

Fan, M., Feng, R., Geissman, J. W et al., Late Paleogene emergence of a North American loess plateau [J] (2020).Geology, 48(3), 273-277.

摘要: 构造运动和全球气候变化在广泛黄土沉积的水文气候形成时所扮演的角色仍然存在争议。先前的研究揭示美国西部渐新世已存在黄土, 但它的时空模式和成因仍然是未知的。本研究通过集成新的地层学资料, 发现在晚始新世中央落基山脉黄土出现的时间变化, 在始新世-渐新世转换期黄土向东扩张到大平原。气候模型的结果揭示, 稳健抬升的北美南部科迪勒拉山使得科迪勒拉冰盖的中部和前沿开始干旱, 形成了尘土潜在的源和汇。在始新世-渐新世转换期的全球变冷驱使北美季风回退而强化了干燥和向东的风尘沉积。因此在晚第三纪末, 风尘沉积反映了由区域构造作用和全球气候变化诱导的大陆干旱化。

ABSTRACT: The relative roles of tectonics and global climate in forming the hydroclimate for widespread eolian deposition remain controversial. Oligocene loess has been previously documented in the interior of western United States, but its spatiotemporal pattern and causes remain undetermined. Through new stratigraphic record documentation and data compilation, we reveal the time transgressive occurrence of loess beginning in the latest Eocene in the central Rocky Mountains, that expands eastward to the Great Plains across the Eocene- Oligocene transition (EOT). Our climate simulations show that moderate uplift of the southern North America Cordillera initiated drying in the Cordilleran hinterland and immediate foreland, forming a potential dust source and sink, and global cooling at the EOT expanded the drying and eolian deposition eastward by causing retreat of the North American Monsoon. Therefore, the eolian deposition reflects continental aridification induced both by regional tectonism and global climate change during the late Paleogene.

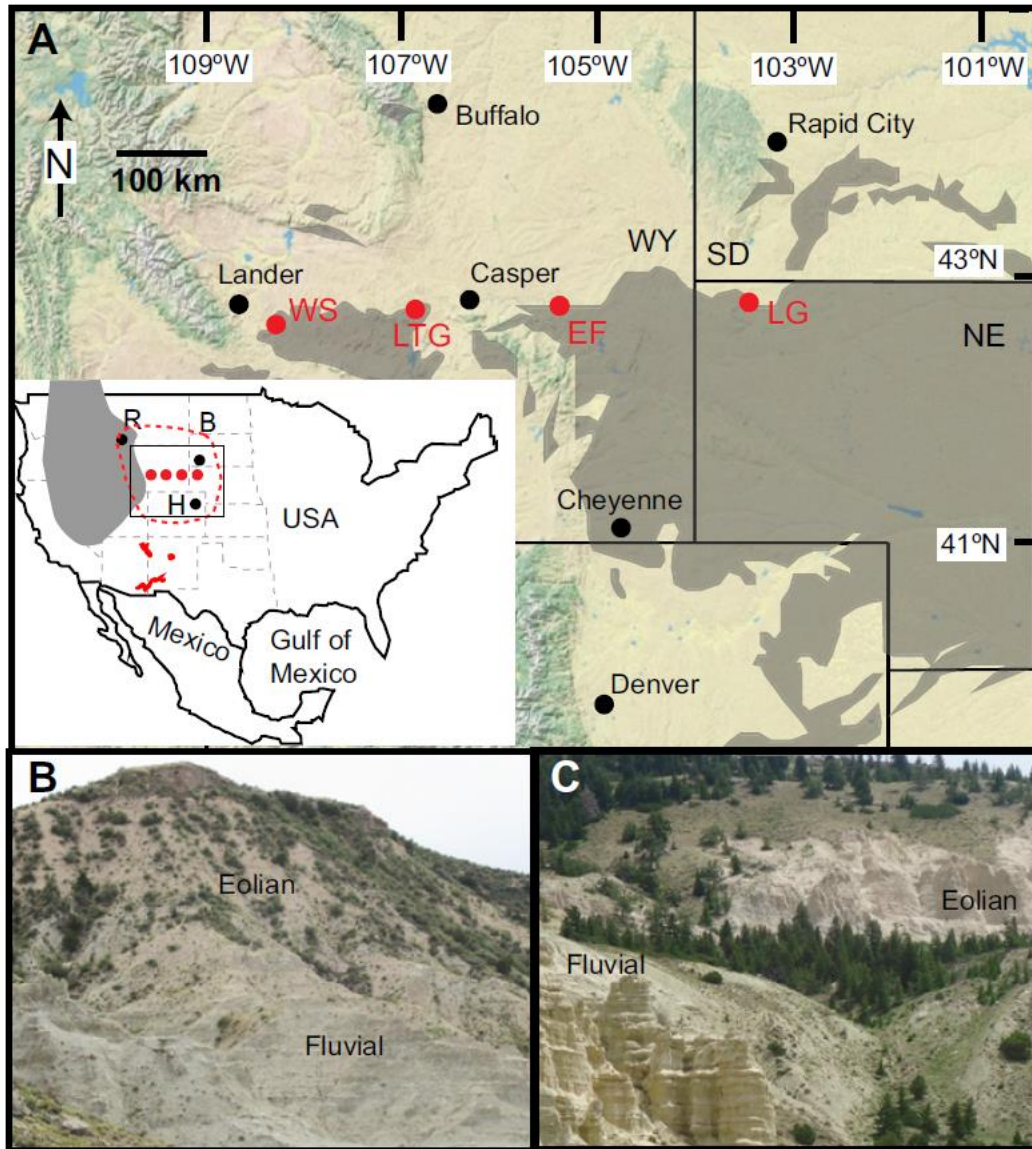


Figure 1. (A) Map of the study area in the central Rocky Mountains and adjacent Great Plains, western USA. Red dots represent the four study sites in this study: WS in Beaver Divide, LTG in Flagstaff Rim, and EF near Douglas in Wyoming, and LG in the Toadstool Geologic Park in Nebraska. Gray areas represent distribution of late Paleogene sedimentary rocks. Inset: The inferred late Paleogene loess plateau is highlighted by the red dashed polygon, based on this study and three other studies: B-Benton et al. (2015), H-Hembree and Hasiotis (2007), R-Robinson (1963). The Chuska erg inferred by Cather et al. (2008) is shown in red polygons, and the Cordilleran hinterland is shown in gray polygon. (B) Field views of the transition from fluvial to eolian deposition in the WS section. (C) Transition to eolian deposition in the EF section. The underlying fluvial units contain interbedded sandstone, conglomerate, and mudstone, and the overlying eolian units are massive. GPS locations of the four study sites are provided in the Data Repository (see footnote 1).

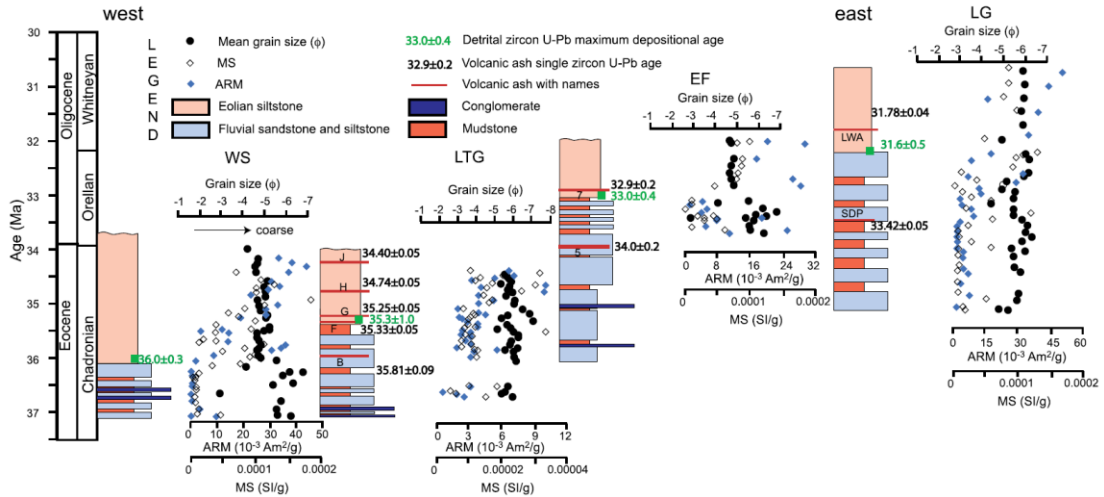


Figure 2. Mean grain-size and bulk magnetic susceptibility (MS) and anhysteretic remanent magnetization (ARM) intensity data collected from the WS, LTG, EF, LG study sites in the western United States are placed in a chronostratigraphic framework for each section. Compiled maximum depositional ages based on detrital zircon U-Pb geochronology, radiometric ages of ash beds (J, H, G, 5, 7, LWA, SDP), and North American Land Mammal Ages (NALMAs) are labeled along each stratigraphic column and illustrate the eastward diachronous initiation of eolian deposition. Note that rocks with a mean grain size larger than medium sand are abundant in the fluvial lithofacies, but were not collected for grain-size analysis. See the text for references, and Fig. DR1 (see footnote 1) for grain-size sorting and bulk saturation isothermal remanent magnetization (SIRM) trends.

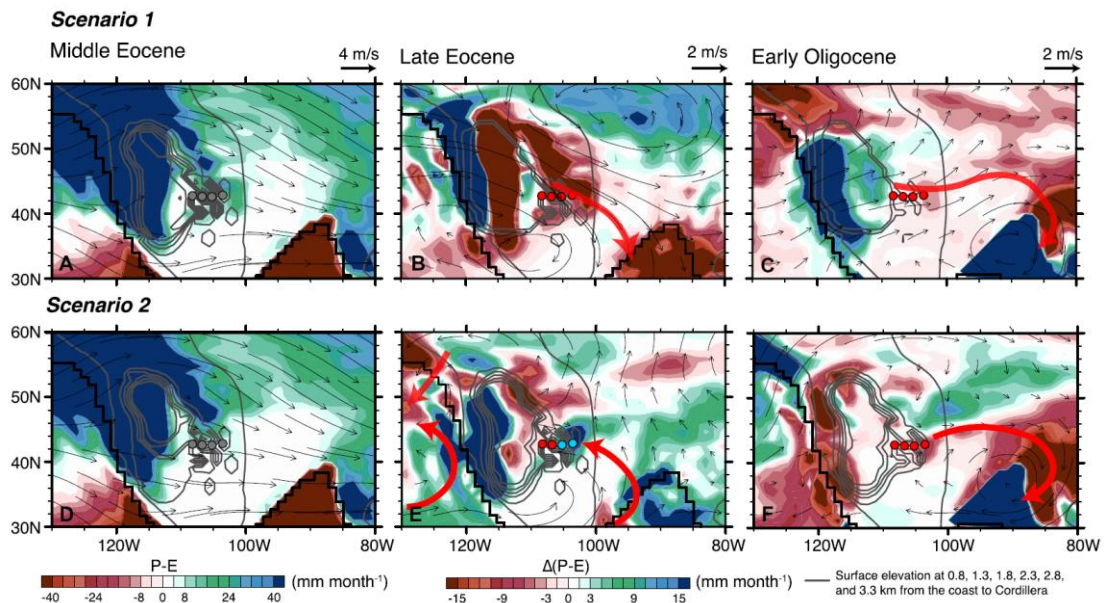


Figure 3. Climatologies simulated for two topographic scenarios featuring North America Cordillera elevation drop (A-C) and southern Cordillera uplift (D-F). Middle Eocene (A and D) is the control case. Response of atmospheric moisture balance is measured by subsequently subtracting simulations of the middle Eocene from simulations of the late Eocene (B and E), and simulations of the early Oligocene from the late Eocene (C and F). Climatologies of models C and F are the

combined results of Eocene-Oligocene transition (EOT) cooling, shoreline regression, and the filling up of Laramide intermontane basins (C and F). Vectors show simulated 700 hPa wind responses of mean annual climatology (A and D) and anomalies (B, C, E, F). Colored dots show precipitation minus evaporation (P-E) changes at the four study (proxy) sites in the western United States, with red representing aridification and blue representing wetting. Red arrows highlight the main changes in the moisture transport path.

4. 皮托深渊 (Pito Deep) 辉长岩的结构特征揭示出快速扩张洋中脊上深成地壳的岩浆过程和起源

翻译人: 李园洁 liyj3@sustech.edu.cn



Brown T C, Cheadle M J, John B E, et al. Textural Character of Gabbroic Rocks from Pito Deep: a Record of Magmatic Processes and the Genesis of the Upper Plutonic Crust at Fast-Spreading Mid-Ocean Ridges[J]. Journal of Petrology, 2019, 60(5): 997-1026.

摘要: 南太平洋皮托深渊(Pito Deep)的结构窗, 可提供机会来研究东太平洋隆起辉长岩洋壳最上部的形成过程。本文我们对暴露在皮托深渊的深成地壳最上部~800 m 的 17 个辉长岩样品进行详细的显微结构和晶体学研究。我们综合晶体大小、形状、空间分布和方向的二维和三维的观测结果, 以及岩相学和地球化学数据来约束快速扩张的辉长岩洋壳的形成过程。席状岩墙之下 (mbsd) < 55 m 采集到的最浅部的样品, 具有块状岩石成分, 细长斜长石晶体, 明显的斜长石形状和晶体学优势取向, 并且仅保留少量晶体内应变。这些岩石和周围的席状岩墙综合体的特征, 表明它们是轴向熔融晶状体的侧面尖端处结晶形成的, 这些晶状体是离开轴时固化的。之下 96-724 mbsd 的样品, 记录了更多原始块状岩石成分, 较少细长斜长石晶体, 并且随着席状岩墙之下深度的增加, 斜长石形状和晶体优势取向增强。这些样品中包含有斜长石晶体, 晶体内应变随深度增加而增加, 说明轴向熔融晶状体下方糊状区内存在岩浆流到超固相亚岩浆流。这些观测结果结合~180 mbsd 之下存在倾斜到陡峭的矿物层, 可解释为记录了起源于 EPR 糊状区最上几千米的熔融晶体的富含晶体的岩浆向下传输的过程。沿着轴向熔融透镜体底部的初始结晶位置决定了影响富含晶体的岩浆固化成为下洋壳的岩浆过程。

ABSTRACT: The tectonic window at Pito Deep, in the southern Pacific Ocean, permits study of the formative processes of uppermost East Pacific Rise (EPR) gabbroic ocean crust. Here we present a detailed microstructural and crystallographic study of 17 gabbroic samples from the uppermost ~800 m of plutonic crust exposed in the Pito Deep Rift. We integrate two- and three-dimensional measurements of crystal size, shape, spatial distribution, and orientation, with petrographic observations and geochemical data to constrain the formation of fast spread gabbroic ocean crust. The shallowest samples, collected < 55 meters below the sheeted dikes (mbsd), have evolved bulk-rock compositions, elongate plagioclase crystals, a clear plagioclase shape- and crystallographic

preferred orientation, and preserve only minor amounts of intracrystalline strain. The characteristics of these rocks, and their proximity to the sheeted dike complex, suggests they formed by crystallization at the lateral tip of an axial melt lens that solidified as it moved off axis. Underlying samples from 96-724 mbsd, record more primitive bulk-rock compositions, less elongate plagioclase crystals, and exhibit increasing strength of both plagioclase shape- and crystallographic preferred orientation with depth below the sheeted dikes. These samples host plagioclase crystals that show increasing intracrystalline strain with depth, suggesting magmatic to hypersolidus submagmatic flow within the mush zone beneath the axial melt lens. These observations, together with inclined-to-steeply dipping mineral layering preserved below ~180 mbsd, are interpreted to record the downward transport of crystal-rich magma originating at the bottom of the melt lens through the uppermost kilometer of the mush zone at the EPR. The location of initial crystallization along the floor of the axial melt lens determines the magmatic processes that affect the crystal-rich magma en route to solidification as lower ocean crust.

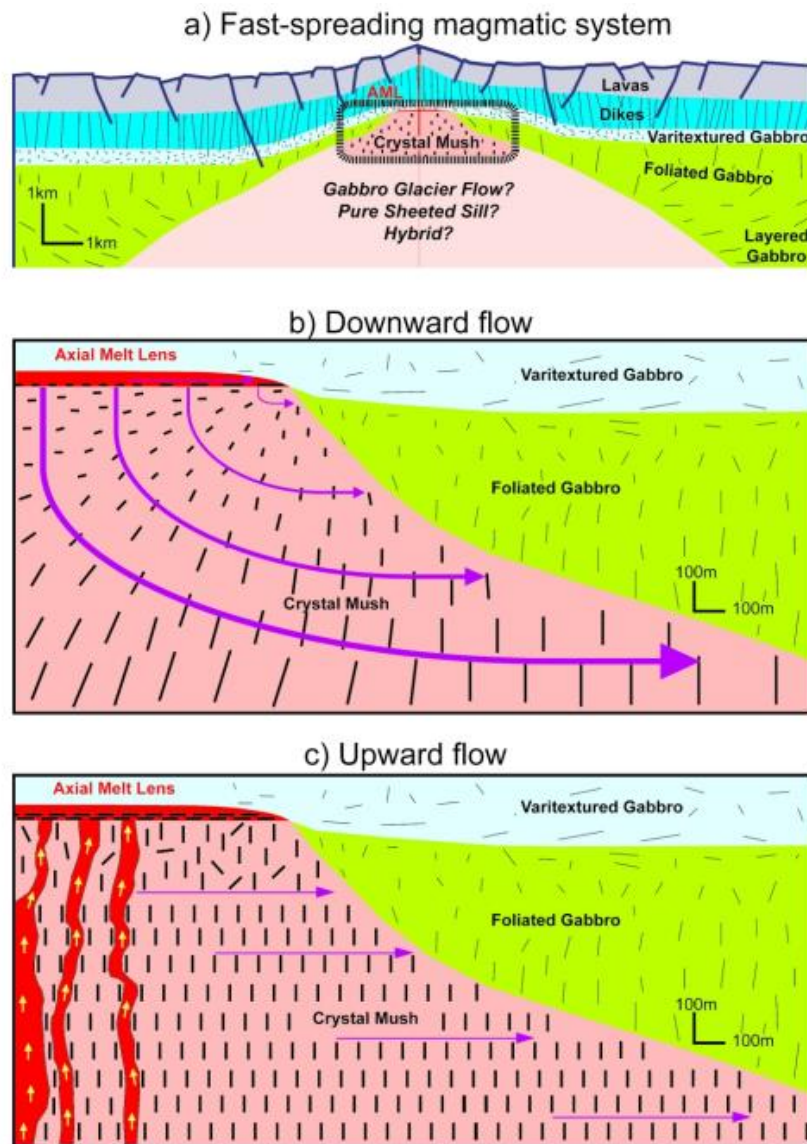


Figure 1. (a) Generic model for the magmatic system at a fast-spreading ridge. Rock types listed are based on the Penrose model (1972) and recent work in the Oman ophiolite (e.g. Yaouancq & MacLeod, 2000; Nicolas et al., 2009). Thin lines in the gabbroic section (green) indicate dominant orientations of the rock fabric as defined by the planar orientation of elongate minerals. Dashed box shows area of focus for this study; the models depicted in (b) and (c) are only for the upper kilometer of the magma system; (b) Downward flow is invoked in gabbro glacier, hybrid, and even some sheeted sill models (e.g. Sleep, 1975; Henstock et al., 1993; Quick & Denlinger, 1993; Boudier et al., 1996; Kelemen et al., 1997). Downward flow in the uppermost kilometer of the magma system suggests that bulk crystallization occurs in the melt lens and crystals are then transported down through the mush. This downward flow creates inclined and steeply dipping fabrics (dashes) preserved in the solidified plutonic crust as the distal tips of the AML and mush zone move off-axis. Purple arrows show crystal mass transport directions through the mush; arrow size approximates distance traveled; (c) Upward flow mechanism applies only to a specific version of the sheeted sill model (e.g. MacLeod & Yaouancq, 2000) and suggests that bulk crystallization initiates and continues in situ throughout the upper kilometer of the magmatic system. Melt migrates upwards (small yellow arrows) to the axial melt lens via flow channels, causing preferential vertical alignment of crystals imparting a vertical foliation in the solidified plutonic crust.

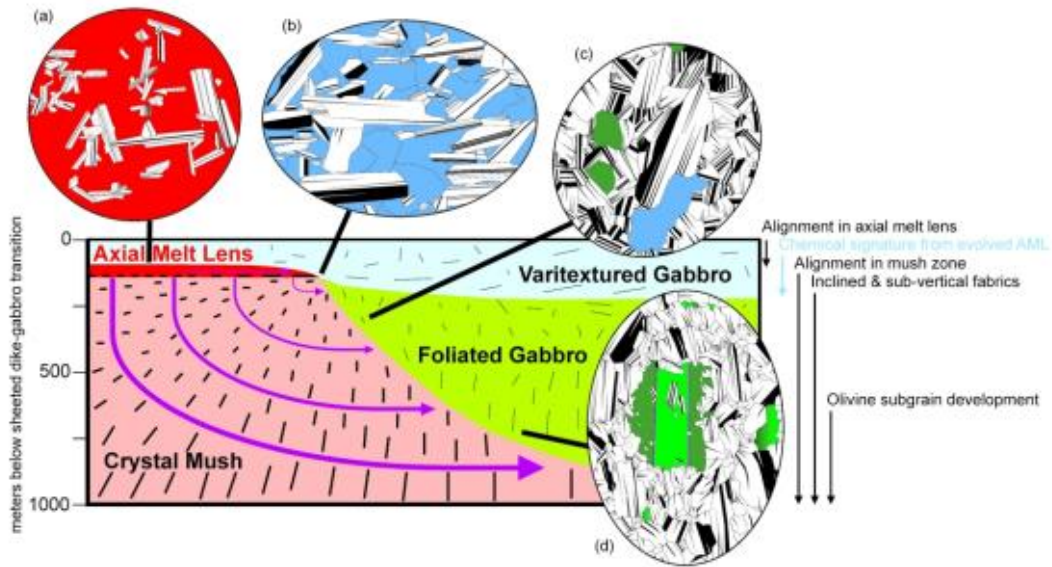


Figure 2. Downward flow model for accretion of upper gabbroic crust at fast-spreading midocean ridges. Purple arrows show the direction of magmatic and sub-magmatic flow. Short black lines beneath the melt lens and in the mush zone indicate the orientation and relative strength (by length) of magmatic foliations formed during subsidence. Overall trends in geochemistry and rock fabric development shown at right; below ~150 mbsd samples are consistently less evolved (blue arrow) than above. Inset bubbles show degree of crystal alignment and stages of textural development from the melt lens to fully solidified gabbroic rocks: (a) Elongate plagioclase initially crystallizes as clustered clots in the melt-rich (red) environment of the AML. (b) Elongate plagioclase aligned by melt-lubricated flow in the AML continues to grow amidst ophitic clinopyroxene crystals (blue). Note minor intra-crystalline strain preserved as tapered twins in plagioclase. (c) Weak steeply dipping magmatic fabric defined by large plagioclase crystals with more plastic strain than adjacent smaller crystals. Olivine (green) does not exhibit internal strain, while elongate pyroxene (blue) parallels the weak plagioclase preferred orientation. (d) Large plagioclase crystals surrounded by smaller, more equant plagioclase crystals forming a steeply dipping fabric. Note the abundant intracrystalline strain preserved in the plagioclase crystals in the form of tapered twins and bent crystals, and in the olivine crystals (green) in the form of sweeping undulatory extinction and sub-grain walls (purple dashed lines separating different green domains). Note the smaller overall crystal size, and the greater proportion of the smallest crystals relative to (b) and (c) despite the longer path/time to solidification. Plagioclase chadacrysts also do not exhibit the degree of deformation that plagioclase in the matrix does, implying that intra-crystalline strain happens early in the mush and continues through oikocryst growth to complete rock solidification.

5. 四国盆地半远洋沉积物的 Sr-Nd-Pb 同位素组成——对新生代晚期黑潮搬运沉积物和菲律宾海板块运动的影响



翻译人: 刘伟 ineway@163.com

Yu Saitoh et al. Sr, Nd, and Pb isotope compositions of hemipelagic sediment in the Shikoku Basin: Implications for sediment transport by the Kuroshio and Philippine Sea plate motion in the late Cenozoic [J]. Earth and Planetary Science Letters, 2015,421:47-57.

摘要: 通过 IODP-C0011 孔晚中新世(7 Ma)至今的碎屑沉积物 Sr-Nd-Pb 同位素组成随时间的变化,研究了四国盆地晚新生代半远洋沉积物的物源。C0011 孔的碎屑沉积物被认为是起源于日本西南弧和中国东海附近陆地的混合沉积物。来源于中国东海的沉积物由黑潮搬运,来源于日本的沉积物由浊流、底流和大洋表层流搬运。同位素证据表明,半远洋沉积物的主要来源从 4.4 Ma 到 2.9 Ma 由中国东海向日本逐渐改变,响应于这一时期菲律宾海板块的北向移动。同时,沉积物粒度大小的增加也支持这一解释。这些变化的起始时期为 4.4 Ma,与四国盆地岩石圈向海沟的俯冲开始时间或加速时间密切相关。

ABSTRACT: The provenance of hemipelagic sediments in the Shikoku Basin during late Cenozoic time was studied through the temporal variations in the Sr-Nd-Pb isotopic compositions of detrital sediments from Integrated Ocean Drilling Program Site C0011 from the late Miocene (7 Ma) to the present. Detrital sediments at Site C0011 are interpreted as a mixture of sediments originating from the southwest Japan arc and lands around the East China Sea. Sediments from the East China Sea were transported by the Kuroshio, while Japanese sediments were transported by turbidity currents, bottom currents, and ocean surface currents. The isotopic evidence suggests that the main source of hemipelagic sediments gradually changed from the East China Sea to Japan from 4.4 to 2.9 Ma, in accordance with the northward movement of Site C0011 with the Philippine Sea plate in this period. A contemporaneous increase in grain size also supports this interpretation. The beginning period of these changes, 4.4 Ma, conforms closely to the postulated advent or acceleration of trench-normal subduction of the Shikoku Basin lithosphere.

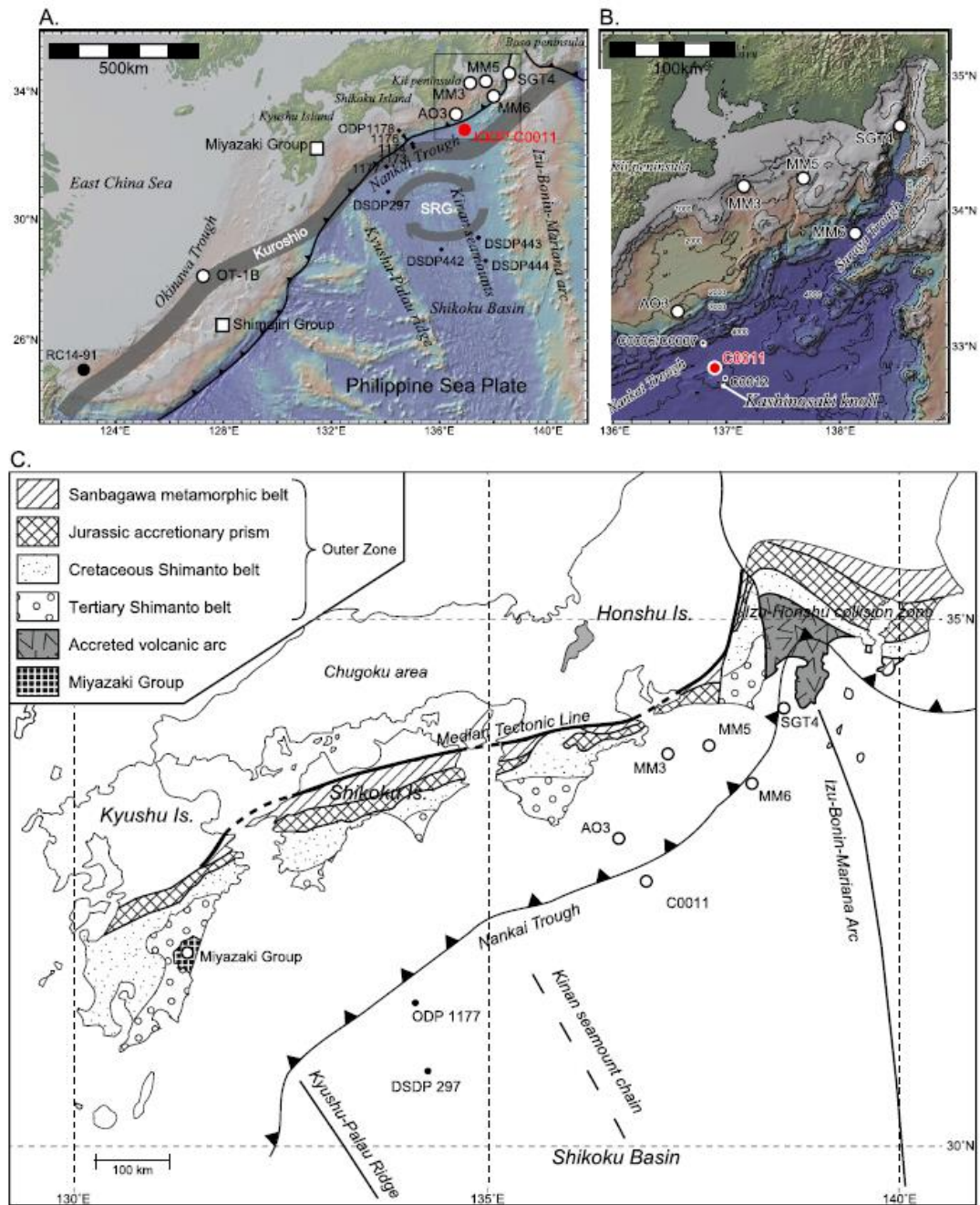


Figure 1. A. Location of the sites, at which samples used in this study were taken. Bathymetry is from GeoMapApp (Ryan et al., 2009). Red circle, the IODP Site C0011 drill hole; white circle, seafloor sediments; white square, outcrop samples, black large circle, seafloor sediments used in Bentahila et al.(2008), of which isotopic compositions of Sr and Pb are referred in this study; black small circle, DSDP and ODP drill halls. SRG, Shikoku Recirculation Gyre. B. Detailed bathymetry around the Site C0011. C. Geology of the Pacific side of southwest Japan Arc (modified after Shipboard Scientific Party, 2001). (For interpretation of the references to color in this figure legend, the reader is referred to the web version of this article.)

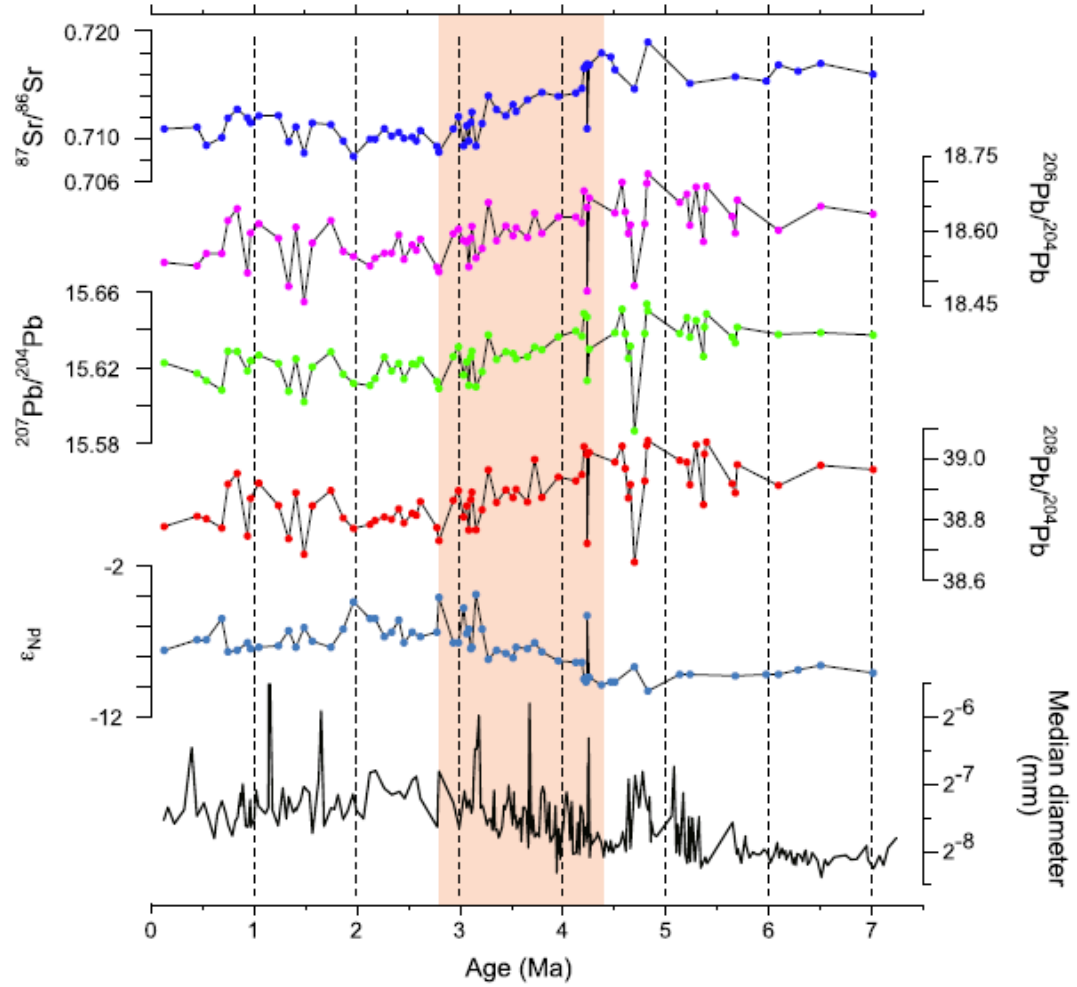


Figure 2. Temporal change of isotope ratios of Sr, Nd, and Pb in silicate component, and median grain diameter of bulk of the C0011 sediment samples. Grain size data is from Saitoh(2014). All isotope ratios and grain size gradually change in the red-shaded period between 2.9 and 4.4Ma. (For interpretation of the references to color in this figure legend, the reader is referred to the web version of this article.)

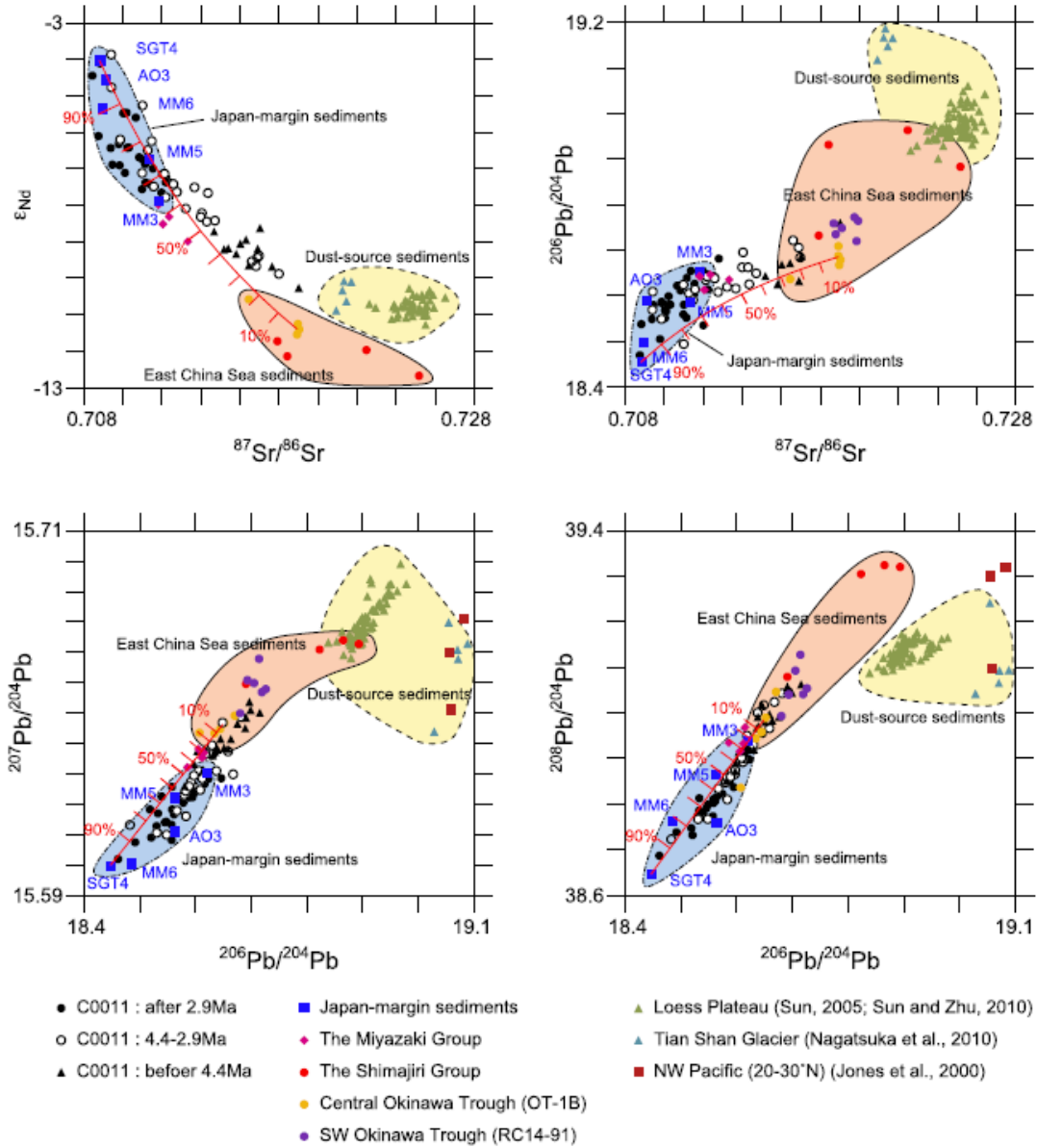


Figure 3. Relationship between isotope ratios. Mixing lines are drawn assuming that the sediments from SGT4 and OT-1B represent those from Japan Arc and the East China Sea, respectively. Japanese contribution is indicated along the lines in percentage terms.

6. 南半球在过去 1Ma 对南亚季风降水的驱动



翻译人: 杨会会 11849590@mail.sustech.edu.cn

D Gebregiorgis, E C Hathorne, L Giosan, et al. Southern Hemisphere forcing of South Asian monsoon precipitation over the past ~1 million years[J]. Nature Communications, 2018, 9: 4702

摘要: 目前对轨道尺度的南亚季风降水的了解还不够深入。本文提供了来自孟加拉湾南亚季风核心对流区在过去 1Ma SST 和海水 $\delta^{18}\text{O}$ 的新数据。我们的数据表明南亚季风降水在北半球夏季太阳辐射岁差周期的最大值后约 9 kyrs 达到峰值, 与阿拉伯海和东印度洋记录的南亚季风一致。然而, 岁差周期的变化只能解释南亚季风降水变率总变化量的 30%, 而在东亚季风的记录中, 它要么是不存在的, 要么是占主导地位。南亚季风降水与地球地转轴周期的最小值同相相关, 且对南半球变暖很敏感, 这一现象为南亚季风和东亚季风降水对轨道驱动响应存在显著区别提供了重要证据, 并强调了影响季风变化的内部过程的重要性。

ABSTRACT: The orbital-scale timing of South Asian monsoon (SAM) precipitation is poorly understood. Here we present new SST and seawater $\delta^{18}\text{O}$ ($\delta^{18}\text{O}_{\text{sw}}$) records from the Bay of Bengal, the core convective region of the South Asian monsoon, over the past 1 million years. Our records reveal that SAM precipitation peaked in the precession band ~9 kyrs after Northern Hemisphere summer insolation maxima, in phase with records of SAM winds in the Arabian Sea and eastern Indian Ocean. Precession-band variance, however, accounts for ~30% of the total variance of SAM precipitation while it was either absent or dominant in records of the East Asian monsoon (EAM). This and the observation that SAM precipitation was phase locked with obliquity minima and was sensitive to Southern Hemisphere warming provides clear evidence that SAM and EAM precipitation responded differently to orbital forcing and highlights the importance of internal processes forcing monsoon variability.

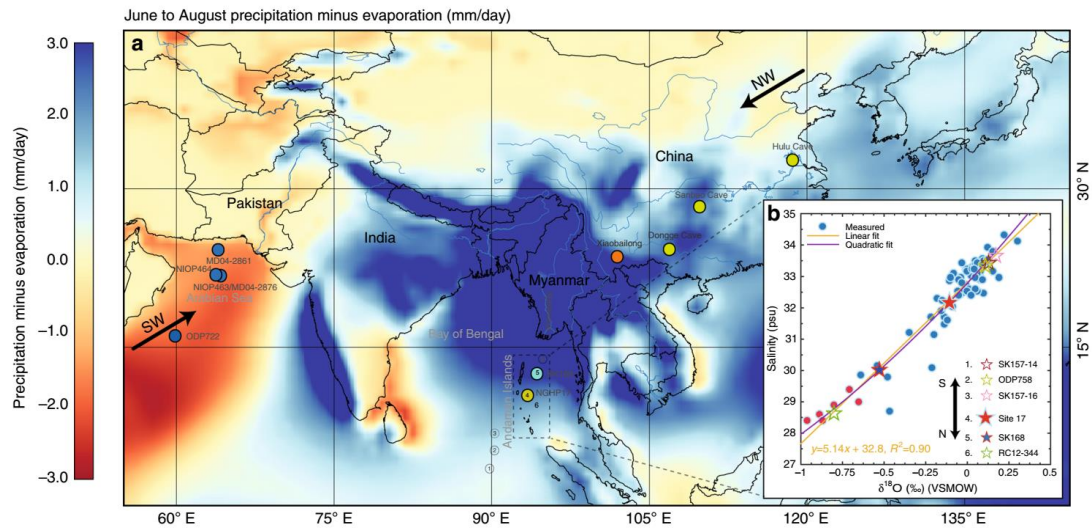


Figure 1. Summer net precipitation in the Asian monsoon domain and modern day salinity and $\delta^{18}\text{O}_{\text{sw}}$ measurements. a Precipitation minus evaporation (mm/day) in the Asian monsoon domain for the period 1979–2015 (precipitation and evaporation data from ERA-Interim global reanalysis dataset). Andaman Sea core sites NGHP 17 (ref. 27) and SSK 168 (refs. 28,29) are shown in yellow and dark green-filled circles. Filled circles show cave and core locations from mainland China^{15,19}, the Arabian Sea^{9,10} and the equatorial eastern Indian Ocean (ODP758)¹³. b Paired $\delta^{18}\text{O}_{\text{sw}}$ and salinity measurements from surface water samples collected from the Andaman Islands in 2011 and 2013 (see Methods) and estimates of $\delta^{18}\text{O}_{\text{sw}}$ calculated based on planktic foraminifera late Holocene (0–2 kyrs) $\delta^{18}\text{O}$ values and modern day mean annual SST⁵⁰ (see Methods for $\delta^{18}\text{O}$ –temperature calibration equation) for six core locations along the N-S transect shown in black circles with numbers (see legend). Measured $\delta^{18}\text{O}_{\text{sw}}$ values shown in red-filled circles are from Achyuthan et al.⁵¹ and are collected close to the Andaman Islands in December 2008.

7. 基于多旋翼无人机的低空地球物理磁勘探有望取代传统的地面勘测



翻译人：曹伟 11930854@mail.sustech.edu.cn

Parshin, Alexander V, Morozov, Vladimir A, Blinov, Anton V et al. **Low-altitude geophysical magnetic prospecting based on multirotor UAV as a promising replacement for traditional ground survey**[J]. *Geo Spatial Information Science*, 2018:1-8.

摘要：在许多国家，扩大矿产资源开发的前景与自然条件复杂的未勘探滞留区域有关，而在这些区域开展磁法勘探等地面调查十分困难且成本昂贵。当前的地质调查的第一阶段需要高精度大规模的数据。自 2012 年以来，无人机航磁测量技术进入市场，但大多基于大型固定翼无人机，与传统航磁测量方法相比，无法大幅提高测量精度。为了扩大测量规模，必须降低飞行高度和速度，本文所研究的就是这些方法和技术解决方案。为了获得地表（即使在崎岖不平的地形上）以上 5 米高度的数据，我们制造了重型多旋翼无人机，这些无人机飞行稳定，可在广泛的环境条件下使用（即使是中等降雪），同时开发了一个基于数字高程模型生成飞行任务的专用软件。无人机采用特殊设计，以减少飞行平台的磁干扰；并且将磁传感器悬挂在飞机下方。这项技术在 2014 年至 2016 年间广泛应用于东西伯利亚山区的磁测。本文展示了航空测量和地面测量的对比结果，结果表明，与低空测量相结合开发的系统灵敏度可以覆盖任何地质意义上的磁场异常。无人机磁测的勘测成本更低，效率更高；基于多旋翼的技术很有可能会取代传统的 1:10000-1:1000 比例尺的地磁勘探。

ABSTRACT: The prospects for expanding the mineral resource base in many countries are linked with the exploration of stranded sites localized at unexplored areas with complex natural and landscape conditions that make any ground survey, including magnetic prospecting, difficult and expensive. The current level of geology requires high-precision and large-scale data at the first stages of geological exploration. Since 2012, technologies of aeromagnetic surveying with unmanned aircraft vehicles (UAV) enter the market, but most of them are based on big fixed-wing UAV and do not allow to substantially increase the level of survey granularity compared with traditional aerial methods. To increase the scale of survey, it is necessary to reduce the altitude and speed of flight, for which the authors develop the methodical and technical solutions described in this article. To obtain data at altitudes of 5 m above the terrain even in a rugged relief, we created

heavy multirotor UAVs that are stable in flight and may be used in a wide range of environmental conditions (even a moderate snowfall), and develop a special software to generate flight missions on the basis of digital elevation models. A UAV has special design to reduce magnetic interference of the flight platform; the magnetic sensor is hung below the aircraft. This technology was conducted in a considerable amount of magnetic surveys in the mountainous regions of East Siberia between 2014 and 2016. The results of the comparison between airborne and ground surveys are presented, which show that the sensitivity of the developed system in conjunction with low-altitude measurements can cover any geologically significant anomalies of the magnetic field. An unmanned survey is cheaper and more productive; the multirotor-based technologies may largely replace traditional ground magnetic exploration in scales of 1:10,000–1:1000.



Figure 1. “Heavyweight” multirotor with magnetometer in flight.

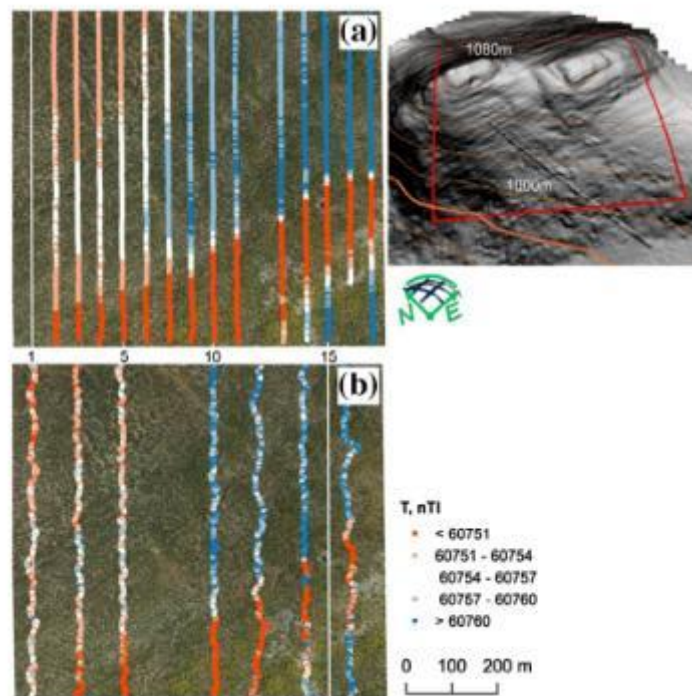


Figure 2. “Heavyweight” multirotor with magnetometer in flight.

8. 利用石笋中细菌 3-羟基脂肪酸对中国中部全新世古温度和古水文变化的重建

翻译人：王敦繁



Canfa W, Bendle J A, Hongbin Z, et al. *Holocene temperature and hydrological changes reconstructed by bacterial 3-hydroxy fatty acids in a stalagmite from central China*[J]. *Quaternary Science Reviews*, 2018, 192:97-105.

摘要：为了进一步认识和理解地球系统气候变化的空间动力学特征，探求能够反应千年尺度及至今时间尺度的新气候变化指标和数据网络是十分必要的。本研究第一次展示了基于全球古气候记录的革兰氏阴性细菌 3-羟基脂肪酸(3-OH-FA)的温度和水文记录。这些来自中国中部长江支流河上洞采集的单个石笋数据覆盖了距今 9 ka 的气候信息。我们的结果表明，全新世早期至中期气候最适宜(8.0-6.0 ka BP)，随后是长期的单调降温，并在过去 0.9 ka BP 的基础上变化增加。水文记录显示，华中地区有两个相对较长的湿润期(8.8-5.9 ka BP 和 3.0-0 ka BP)和一个相对干旱期(5.9-3.0 ka BP)。我们发现，3-OH-FA 生物标记物有望成为重建古气候的独立工具，有望帮助人们更好的理解单个石笋中关于古气候的温度和水文信号记录。

ABSTRACT: To achieve a sufficient understanding of the spatial dynamics of terrestrial climate variability, new proxies and networks of data that cover thousands of years and run up to the present day are needed. Here we show the first Gram-negative bacterial 3-hydroxy fatty acid (3-OH-FA) based temperature and hydrological records from any paleoclimate archive globally. The data, covering the last 9 ka before present (BP), are generated from an individual stalagmite, collected from Heshang Cave, located on a tributary of the Yangtze River, central China (30°27' N, 110°25' E; 294 m). Our results indicate a clear early- to-middle Holocene Climatic Optimum (8.0-6.0 ka BP) followed by a long-term monotonic cooling and increasing variability over the last 0.9 ka BP. The hydrological record shows two relatively long wet periods (8.8-5.9 ka BP and 3.0-0 ka BP) and one relatively dry period (5.9-3.0 ka BP) in central China. We show that 3-OH-FA biomarkers hold promise as independent tools for paleoclimate reconstruction, with the potential to deconvolve temperature and hydrological signals from an individual stalagmite.

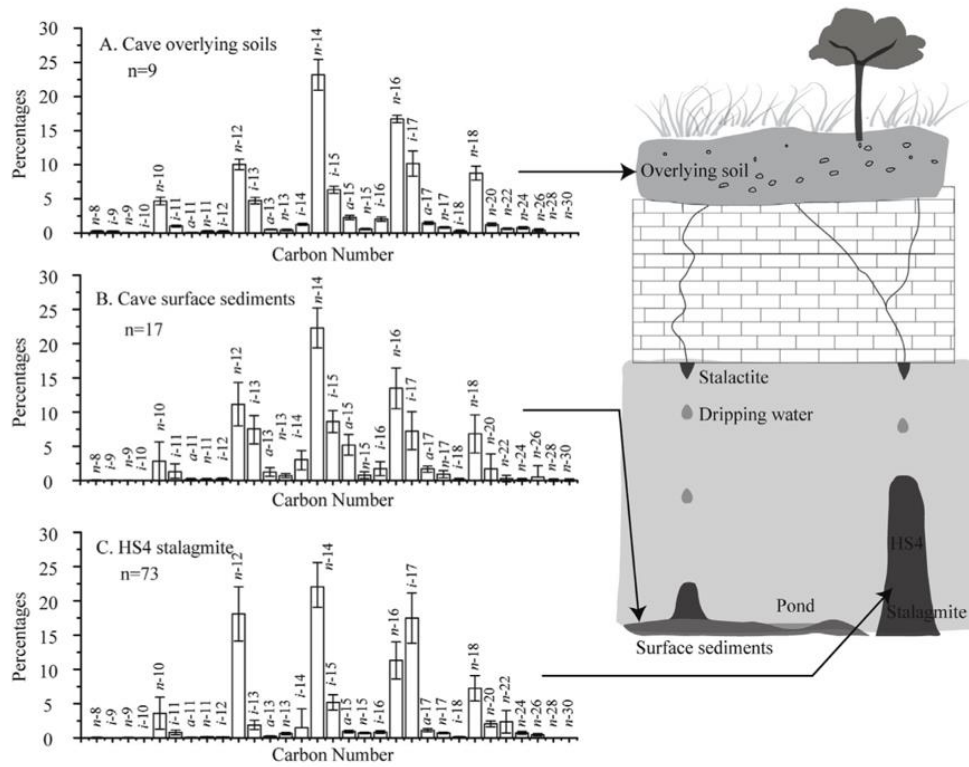


Figure 1. Distribution and fractional abundance of 3-hydroxy fatty acid homologues in (A) cave overlying soils, (B) cave surface sediments, and (C) HS4 stalagmite samples.

9. 西班牙 Busturia 的 Goikoetxe 洞穴沉积物红色着色：对古气候变化的指示



翻译人：郑威 11930589@mail.sustech.edu.cn

Martínez-Pillado V, Yusta I, Iriarte E, et al. The red coloration of Goikoetxe Cave's speleothems (Busturia, Spain): An indicator of paleoclimatic changes[J]. Quaternary International, 2020.

摘要：方解石的碳氧同位素和微量元素是在洞穴沉积物研究中最常使用的古气候代用指标。然而，综合评估其它组成，例如有机质，也可能对解译和重建洞穴沉积物生长时期的气候有意义。本研究认为来源于上覆土壤的腐殖酸和富里酸是导致Goikoetxe洞穴沉积物出现红色的原因。应用岩石学研究，并结合X射线荧光、紫外冷光、拉曼光谱和红外光谱傅里叶变换分析，作者认为上覆土壤的有机质含量变化与洞穴沉积物出现红色可能相关，这种染色是研究和重建季节性古气候参数的主要代用指标。

ABSTRACT: The most commonly used paleoclimatic proxies in speleothem studies are the carbon and oxygen stable isotopes and the trace elements of calcite. However, assessing the incorporation of other components, such as organic matter, may also be of interest in interpreting and reconstructing the climate during speleothem growth. In this work, the incorporation of humic and fulvic acids derived from overlying soils is proposed as the cause of the red coloration of speleothems from the Goikoetxe Cave (Busturia, Bizkaia). Through the application of petrological studies combined with X-ray fluorescence, UV luminescence, Raman spectroscopy and Fourier-transform infrared spectroscopy (FTIR) analysis, it has been possible to correlate a variation of organic content in the overlying soils and the red coloration, being this stain a main proxy to study and reconstruct the seasonal paleoclimatic parameters during the speleothem formation.

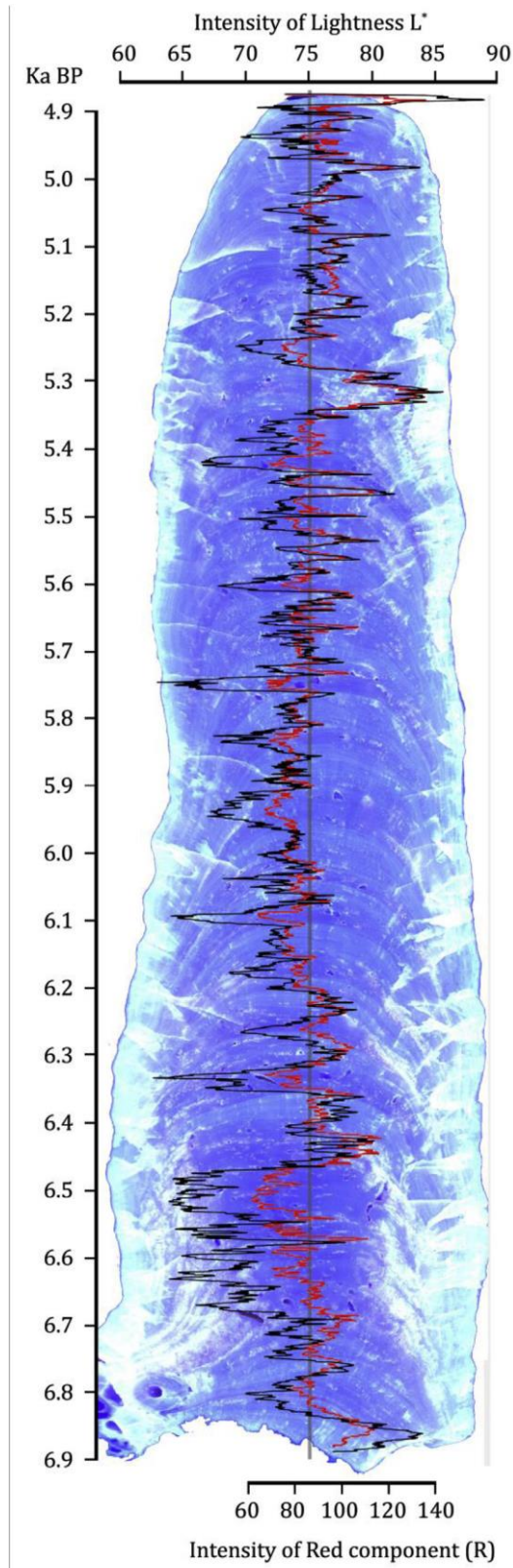


Figure 1. Lightness (L^* , black line) and Red component (RGB, red line) intensity profiles measured over the UV light photograph of Moreno stalagmite through time. The profiles have been measured in the central part of the growth axis. Darkest luminescence bands are associated with high OM content due to selfabsorbance effect (fluorescence quenching). (For interpretation of the references to color in this figure legend, the reader is referred to the Web version of this article.)